



Pd catalysts supported onto nanostructured carbon materials for CO₂ valorization by electrochemical reduction



S. Pérez-Rodríguez^{a,b}, N. Rillo^a, M.J. Lázaro^{a,*}, E. Pastor^b

^a Instituto de Carboquímica (CSIC), Miguel Luesma Castán 4, 50018 Zaragoza, Spain

^b Universidad de La Laguna, Dpto. Química-Física, Avda. Astrofísico Francisco Sánchez s/n, 38071 La Laguna (Tenerife), Spain

ARTICLE INFO

Article history:

Received 18 April 2014

Received in revised form 2 July 2014

Accepted 15 July 2014

Available online 22 July 2014

Keywords:

Carbon nanofibers

Carbon nanocoils

Ordered mesoporous carbon materials

CO₂ electroreduction

Palladium

ABSTRACT

Pd nanoparticles have been supported onto different novel carbon materials to be used in the electroreduction of CO₂ to high-added value products. Carbon nanocoils (CNCs), carbon nanofibers (CNFs) and ordered mesoporous carbon materials (OMCs) have been studied as support of the catalysts. In addition, Pd catalyst supported onto Vulcan XC-72R has been synthesized in order to establish a comparison with the commercial support. In this way, the influence of the carbon material on the physicochemical and electrochemical properties of the catalysts for the CO₂ electroreduction process can be analyzed. Supports presented different morphologies and structures. CNFs and CNCs exhibited a crystalline structure with well-aligned graphitic layers and OMCs a hexagonal ordered structure composed of not crystalline carbon. Finally, Vulcan presented an intermediate structure between amorphous and graphitic. These differences do not affect significantly the average Pd crystallite size, although a different metal dispersion was found depending on the carbon material. On the other hand, cyclic voltammetry studies showed that CO₂ was effectively reduced to other species at the surface of Pd/C catalysts. Additionally, it was proved that these species were adsorbed onto Pd at −1.0 V vs Ag/AgCl. Finally, a different catalytic activity towards the CO₂ reduction reaction was observed for the different electrocatalysts, indicating an influence of the carbon support.

© 2014 Elsevier B.V. All rights reserved.

1. Introduction

Nowadays, CO₂ is the main responsible of global warming, and therefore, several CO₂ mitigation strategies are being studying. Among them, the CO₂ conversion represents a promising alternative for the reutilization of this gas, with the aim of producing useful products, with important applications in chemical industry and for power generation. Different methods have been carried out to convert CO₂, such as chemical, thermochemical, photochemical, electrochemical and biochemical procedures. The electrochemical route shows a wide selectivity towards valuable products (methane, methanol, monoxide carbon, acid formic, etc.) [1].

Various metallic electrodes have been studied for the CO₂ electrochemical reduction in aqueous solutions, since the catalytic activity and the product distribution depend strongly on the used material and the surface metallic arrangement [2–6]. Copper has attracted special attention [1,2,7–11], due to its exceptional selectivity for CO₂ conversion to hydrocarbons and alcohols at

significant current densities. On the other hand, metals of the group VIII elements, such as Pt and Pd, have been also studied in detail by several authors [12–24], since these electrodes present low hydrogen overpotentials and easily adsorb hydrogen. Adsorbed hydrogen favors the adsorption of species derived from CO₂ on the electrode surface, since the formation of “reduced CO₂” adsorbates requires interaction between CO₂ molecules and adsorbed hydrogen [12,13,16–18]. These adsorbates are expected to play an important role in the reduction pathway of the process, since adsorbed species may behave as both reactive intermediate and poison. Beden et al. revealed by means of infrared spectroscopy, that CO₂ is reduced to CO, which is strongly adsorbed onto Pt, inhibiting further reduction of CO₂ and, therefore, obtaining H₂ (formed by water reduction) as main product [20]. Same behavior was found for the rest of metals of the group VIII elements (Ni, Fe, etc.), excepting Pd [3,25,26]. On this last metal, CO and formic acid have been reported as main products, and even hydrocarbons have been obtained at low current efficiencies [12,15]. Taguchi et al. attributed this different behavior to the higher adsorption affinity of “reduced CO₂” on Pt than on Pd and suggested that “reduced CO₂” would be behaving as a catalytic self-poisoning for the electrochemical reduction of CO₂ on Pt, but it partly becoming an

* Corresponding author. Tel.: +34 976733977; fax: +34 976733318.

E-mail address: mlazaro@icb.csic.es (M.J. Lázaro).

intermediate on Pd [14]. On the other hand, this different activity can be also explained by the differences in the process of hydrogen sorption (adsorption and absorption)/desorption. It is widely known that the bulk absorption of hydrogen in Pt is insignificant in comparison to Pd, under the same conditions [27]. Therefore, a substantial amount of the hydrogen obtained on the Pd electrodes would be bulk absorbed by the metal, lowering the rate of detected hydrogen and changing the adsorption affinity of the species derived from the CO₂ reduction reaction.

Despite all this extended research of the electrochemical reduction of CO₂ on different metallic electrodes, the involved mechanism and the implied intermediates of the reaction are not fully clear, however. Moreover, many limitations must be addressed to make the process viable. One of the main problems is the low solubility of CO₂ in aqueous systems, at atmospheric pressure and room temperature. For this reason, the electroreduction of CO₂ has been also studied onto different metals at high pressure (30–60 atm) [8,28,29], low temperatures (0 to (–30) °C) [4,8–10,30] and/or in aprotic solvents (methanol, acetonitrile, dimethyl sulfoxide, propylene carbonate, etc.) [21,31,32], in order to avoid these mass transport limitations. Despite of obtaining hydrocarbons and more complexes products, the current efficiencies remained being low. In addition, a quick deactivation of the electrodes was observed due to the higher current densities under these conditions [7,11]. In order to partly resolve these issues, the use of gas diffusion electrodes (GDEs) and/or catalysts supported on nanostructured carbon materials has been proposed over the last few decades [21,33–40]. These porous electrodes allow a good distribution of the reactives over the catalyst surface, obtaining a large reaction area while provide low current density with high current efficiency for the formation of products. Additionally, support nanopores help to confine CO₂, resulting in higher pressures at the electrocatalyst surface, which favor the reaction kinetics. It has been found that using electrodes based on carbon materials the product partial current densities are considerably higher than those obtained for the corresponding bulk electrodes, and even the selectivity of the process can be modified. Surprising a mixture of C1–C9 hydrocarbons and alcohols were found in different GDEs based on noble metals supported on modified carbon cloths [36,39]. Pérez-Rodríguez et al. reported the formation of formic acid below –0.7 V vs. Ag/AgCl, at atmospheric pressure and room temperature using iron-oxide electrodes supported on treated Vulcan XC-72R [35], while bulk Fe electrodes produce H₂ as the main product under the same conditions [41]. Mahmood et al. employed a lead-impregnated GDE to reduce CO₂ to formic acid with a current efficiency of nearly 100%, operating at –1.8 V vs. SCE [34].

Most of these studies have been carried out using carbon blacks as support, specifically Vulcan XC-72R, which is the most commonly carbon material used for electrochemical applications, due to its low cost and its good compromise between electrical conductivity and high specific surface area [42]. However, there are not many studies about the electroreduction of CO₂ on catalysts supported on different nanostructured carbon materials, such as carbon nanofibers (CNFs), carbon nanocoils (CNCs), ordered mesoporous carbon materials (OMCs) or carbon nanotubes (CNTs) [33,37,38,40]. These carbon materials present different properties, such as crystallinity, morphology, porosity and surface chemistry than those of the commercial material, Vulcan. Therefore, the mass transport, the conductivity and the electrochemical surface area of the electrocatalysts, as well as size, dispersion and stability of the metallic nanoparticles could be affected. Accordingly the activity and selectivity towards the production of hydrocarbonated compounds from CO₂ would be modified. Hence, the optimization of the carbon materials plays an important role on the CO₂ electroreduction research.

In this work, various Pd catalysts have been synthesized to be tested in the CO₂ electroreduction process. Different novel nanostructured carbon materials, such as CNCs, CNFs and OMCs, have been used as support of the catalysts. In addition, Vulcan XC-72R was also tested in order to establish a comparison with the commercial support. In this way, the influence of the carbon material on the physicochemical and electrochemical properties of the catalysts for the CO₂ electroreduction process can be analyzed. In this context, to the best of our knowledge, this is the first time that CO₂ reduction is carried out using different nanostructured carbon materials as supports, in order to obtain a comparison of them and establish their influence on the activity of the process.

2. Experimental

2.1. Synthesis of the nanostructured carbon materials

2.1.1. Preparation of Carbon Nanofibers (CNFs)

CNFs were grown by methane decomposition over a NiCuAl₂O₃ (molar ratio 78:6:16) catalyst.

The NiCuAl₂O₃ catalyst was prepared by coprecipitation of metal salts, Ni(NO₃)₂·6H₂O (98 wt.%, Alfa Aesar), Cu(NO₃)₂·3H₂O (99 wt.%, Panreac) and Al(NO₃)₃·9H₂O (98 wt.%, Alfa Aesar), and calcination at 450 °C for 4 h. The resultant catalyst precursor was reduced under a H₂ flow of 20 mL min^{–1} at 550 °C during 1 h, obtaining the active phase for the CNFs growing.

The methane decomposition reaction was carried out in a fixed-bed vertical reactor under a pure CH₄ flow (20 mL min^{–1}) at 700 °C during 10 h. Further details can be found elsewhere [43]. Other studies have shown that these conditions result in a high carbon graphitization without catalyst deactivation [44,45].

Finally, CNFs were treated with concentrated nitric acid (65 wt.%, Panreac) at room temperature for 2 h to remove the metal particles. Obtained CNFs were filtered, washed with abundant deionized water and then dried overnight at 80 °C.

2.1.2. Preparation of Carbon Nanocoils (CNCs)

CNCs were synthesized by the catalytic graphitization method, using Ni(NO₃)₂·6H₂O (98 wt.%, Alfa Aesar) and Co(NO₃)₂·6H₂O (98 wt. %, Sigma-Aldrich) metal nitrates as graphitization catalysts, and a mixture of resorcinol (>98 wt.%, Saft) and formaldehyde (37 wt.%, Sigma-Aldrich) as the carbon precursor. Moreover, silica sol (Supelco) was used to generate mesoporosity. The synthesis involved the following steps:

First, formaldehyde and silica sol were dissolved in deionized water. Then, the nickel-cobalt salts and resorcinol were added under mechanical stirring. The molar ratio H₂O/Co nitrate/Ni nitrate/resorcinol/formaldehyde/silica used for the synthesis was 100:0.2:0.2:1:2:0.6 [46]. The obtained mixture was heated, first at 85 °C for 3 h in a closed system, and then at 108 °C. Subsequently, it was carbonized under a N₂ atmosphere at 900 °C for 3 h, and the resultant material was washed with 1.1 M NaOH (98 wt.%, Panreac) solution (an EtOH (96%, v/v, Panreac)–water mixture of 1:0.3 in volume), in order to remove the silica particles.

Finally, CNCs were treated with concentrated nitric acid (65 wt.%, Panreac) at room temperature for 2 h to remove the metal particles. Obtained CNCs were filtered, thoroughly washed with deionized water and then dried overnight at 80 °C [47].

2.1.3. Preparation of Ordered Mesoporous Carbons (OMCs)

OMCs were prepared by the nanocasting technique using a mesoporous silica (SBA-15) as template and a furan resin/acetone as carbon precursor. The synthesis involved the following steps:

First, the template was synthesized using Tetraethyl Orthosilicate (TEOS, 98 wt.%, Aldrich) as silica precursor and Pluronic P123 copolymer (EO₂₀PO₇₀EO₂₀, Aldrich) as mesoporosity creator. With

this purpose, the P123 surfactant was dissolved in a 1.8 M HCl (37 wt.%, Sigma–Aldrich) aqueous solution. The resultant mixture was subjected to heat treatment at 50 °C for 2 h under mechanical stirring. Then, TEOS (with a mass relation TEOS/P123 = 20:4) was dropwise added and the solution was heated 2 h more. The obtained gel was heated at 85 °C during 24 h, followed by a filtration and washing process. The sample was heated overnight at room temperature and then at 108 °C. Finally, the silica was calcinated under a N₂ atmosphere at 500 °C for 5 h in order to eliminate the P123 surfactant and to obtain an ordered mesoporous structure [48].

After, OMCs were prepared from the silica templates. With this finality, the calcinated silica was subjected to incipient-wetness impregnation with the carbon precursor: a mixture of furan resin (furfuryl alcohol and formaldehyde, Huttenes-Albertus) and acetone (99.5 wt.%, Panreac), with a mass relation 5:1. The impregnated silica was heated at 108 °C for 24 h, and then was carbonized under a N₂ atmosphere at 700 °C for 3 h. Subsequently, the resulting material was washed with 1.1 M NaOH (98 wt.%, Panreac) solution (an EtOH (96%, v/v, Panreac)–water mixture of 1:0.3 in volume), in order to remove the silica particles. Obtained OMCs were filtered, thoroughly washed with deionized water and then dried overnight at 80 °C [49].

2.2. Synthesis of the carbon-supported Pd electrocatalysts

The carbon-supported Pd electrocatalysts were prepared by the method of impregnation and reduction with sodium borohydride. The synthesized nanostructured carbon materials (CNFs, CNCs and OMCs) were used as supports. Moreover, Pd catalyst supported onto Vulcan XC-72R (Cabot Corporation), was also prepared in order to establish a comparison with the commercial support.

The synthesis involved the following steps: first, a 3.0 mM metal precursor Na₂PdCl₄ (98 wt.%, Sigma–Aldrich) solution was slowly added to a dispersion of the different carbon materials in ultrapure water under sonication. Afterwards the pH of the dispersion was adjusted to 5.0 using NaOH (98 wt.%, Panreac). Then, the metal was reduced with a 48.0 mM sodium borohydride (99 wt.%, Sigma–Aldrich) solution, keeping the temperature below 18 °C and in the presence of sonication. Finally, catalysts were filtered, washed with ultrapure water (Millipore Milli-Q system), and then dried overnight at 70 °C.

Appropriate amounts of the metal precursor were employed to obtain a theoretical Pd loading of 20 wt.% on the different carbon materials.

2.3. Physicochemical characterization

Carbon materials obtained in the previously described procedures were characterized by different physicochemical techniques like transmission electron microscopy (TEM), X-ray diffraction (XRD) and N₂ physisorption. On the other hand, carbon-supported catalysts (Pd/C) were characterized by energy dispersive X-ray analysis (EDX), thermogravimetric analysis (TGA), TEM and XRD.

Transmission electron microscope (TEM) micrographs for the carbon supports and the Pd electrocatalysts were obtained using a JEOL-2000 FXII microscope equipped with a LaB₆ gun. The samples were grounded, dispersed in ethanol and a drop of solution was then deposited on a copper grid.

X-ray diffraction (XRD) patterns of the materials were recorded using a Bruker AXS D8 Advance diffractometer with a θ – θ configuration and using Cu K α radiation (λ = 0.15406 nm). Scans were done at 1° min^{−1} for 2 θ values from 10° to 80°, for Pd catalysts or graphitic carbon materials (Vulcan, CNFs and CNCs) or at 0.24° min^{−1} for 2 θ values from 0.5° to 4° for OMCs. The graphite interlayer spacing (d_{002}) for crystalline carbons and interplanar distance (d_{100}) for OMCs were calculated from the position of the (002) and (100)

peaks, respectively, applying the Bragg's equation [50,51]. Crystal-lite sizes were calculated from Scherrer's equation on the (002) peak for carbon supports (L_c) and on the (220) peak for Pd (with a K value of 0.89) [51,52]. The graphitization degree of supports (g) was calculated from Mering and Maire equation (validity range: $0.3354 \leq d_{002} \leq 0.3440$ nm) [53,54]. Taking into account the hexagonal structure of OMCs, the unit cell parameter or the distance between the carbon cylinder centers (a) was obtained by using the formula $a = 2 \cdot d_{100} / \sqrt{3}$ [50].

N₂ adsorption–desorption isotherms of the carbon supports were measured at −196 °C using a Micromeritics ASAP 2020. The total surface area was calculated from BET (Brunauer, Emmett and Teller) equation and the total pore volume was determined using the single point method at $P/P_0 = 0.99$. Pore size distribution (PSD) curves were obtained from the analysis of the desorption branch of the N₂ isotherm using the BJH (Barrett, Joyner and Halenda) method.

Metal content of the electrocatalysts were obtained by energy dispersive X-ray analysis and thermogravimetric analysis (TGA) in air. An EDX analyzer Röntec XFlash Si(Li) coupled to a Hitachi S-3400N scanning electron microscope (SEM) was used. TGA experiments were carried out on a thermogravimetric SETARAM Setsys Evolution under air atmosphere. The temperature was varied between room temperature and 950 °C with a heating rate of 5 °C min^{−1}. In order to obtain the metal content of the electrocatalysts, TGA analysis were also carried out for the carbon supports. In this way the Pd load was calculated by the difference between the residual value of the catalysts and the carbon materials, both results obtained by TGA under the same conditions described above.

2.4. DEMS set-up

A scheme of the DEMS setup used for the in situ spectrometric and electrochemical measurements is described in [55]. Briefly, the spectro-electrochemical experiments were carried out in a conventional three electrodes electrochemical cell, directly attached to the vacuum chamber of a mass spectrometer (Balzers Omnistar quadrupole mass spectrometer), with a Faraday cup detector. The working electrode consists of a glassy carbon disk (7.0 mm of exterior diameter, SIGRADUR® G) with an inner cavity of around 1.5 mm of diameter, where a PTFE membrane (Scimat) is accurately placed allowing the detection of volatile and gaseous products and intermediates generated in the electrochemical reactions with excellent sensibility. Further details are given in [55].

In order to carry out spectro-electrochemical measurements properly, the Pd electrocatalysts were dispersed onto the total surface of the carbon disk. Therefore, the designed cell allows to follow “in-situ” the electrochemical properties of electrodes and, simultaneously, the gaseous species produced on the electroactive surface, providing more information than a conventional electrochemical technique (i.e., cyclic voltammetry or chronoamperometry).

2.5. Spectro-electrochemical measurements

Electrochemical measurements were carried out in a three electrodes electrochemical cell at room temperature and atmospheric pressure. The potentiostat–galvanostat was an Autolab PGSTAT302 (Ecochemie). In the case of the spectro-electrochemical measurements, the same cell was directly attached to a mass spectrometer (Section 2.4). In this way, the experimental set-up allows the simultaneous acquisition of mass spectrometric cyclic voltammograms (MSCVs) for selected m/z (mass to charge) ratios and conventional cyclic voltammograms (CVs). In this work, DEMS experiments were carried out to follow the formation of molecular H₂ ($m/z = 2$), simultaneously produced by water reduction during the CO₂ electrochemical reduction.

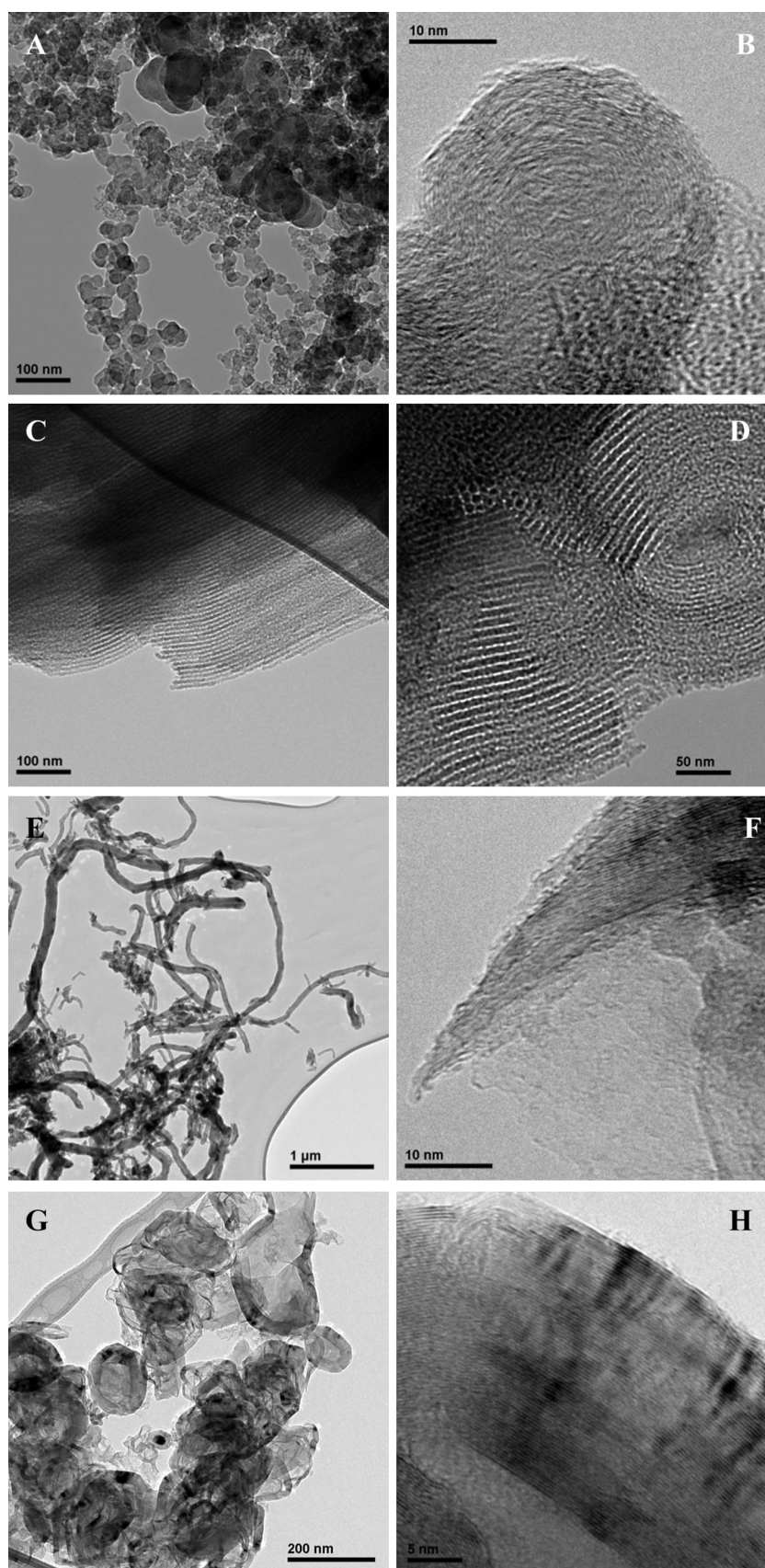


Fig. 1. TEM images of carbon supports: Vulcan (A, B), OMCs (C, D), CNFs (E, F) and CNCs (G, H).

A high surface area carbon rod was used as a counter electrode, whereas an Ag/AgCl/3 M KCl electrode placed inside a Luggin capillary was employed as reference. All potentials in the text are referred to this electrode. The working electrodes were prepared depositing a thin-layer of the different electrocatalysts over the glassy carbon disk (7.0 mm of diameter, SIGRADUR® G) for the electrochemical experiments. In the case of spectro-electrochemical measurements, it was used the carbon disk with the Teflon membrane (7.0 mm of exterior diameter, SIGRADUR® G). Catalyst inks were prepared, in all the cases, by mixing 2 mg of catalyst, 15 μ L of Nafion dispersion (5 wt.%, Aldrich) and 500 μ L of ultrapure water (Millipore Milli-Q system). The suspension was submitted under sonication for 40 min. An aliquot of 10 μ L of the suspension was pipetted onto the carbon disk and dried at room temperature.

The working electrode was immersed into 0.1 M NaHCO₃ (Merck, p.a.) electrolyte solution. Ar (N50) was used to deaerate all solutions and CO (N47) was employed for the adsorption experiences. In order to analyze the activity of catalysts towards the reduction of CO₂, previously to each measure, CO₂ (99.99%, Air Liquide) was bubbled during 30 min, decreasing the pH value of the solution (8.4 in the presence of Ar and 6.8 in the presence of CO₂).

3. Results and discussion

3.1. Physicochemical characterization of the supports

The different morphology of carbon materials was studied by TEM. Vulcan images (Fig. 1A and B) showed that the commercial support is formed by an aggregation of spherical carbon nanoparticles (primary particles) with range diameter sizes of 15–80 nm. In addition, primary particles consist of small crystallites, which are composed of several parallel graphene layers, arranged randomly around the particle with a turbostratic structure (Fig. 1B). These crystallites confer Vulcan a certain crystallinity degree. On the other hand, OMCs exhibit a hexagonal ordered structure, which consists of periodic amorphous carbon cylinders, of around 6 nm of diameter (seen by TEM), with uniform mesopores between them (near 3–4 nm). Fig. 1C displays the parallel disposition of the pores and their hexagonal structure can be seen in Fig. 1D. Finally, CNFs and CNCs show well-aligned graphitic layers (Fig. 1F and H, respectively). CNFs appear as long carbon nanofilaments, with graphene layers oblique to the growth axis or “fishbone” morphology (Fig. 1E) and CNCs as spherical particles composed of several long curved ribbons with a wide diameter distribution (Fig. 1G).

Fig. 2.A shows the XRD patterns of all the carbon supports. All the samples, with the exception of OMCs, show a peak around $2\theta = 25^\circ$, which is associated to the graphite (002) diffraction line. However, some differences between the carbon materials are observed. An increase of the graphitization degree of the carbon supports leads to an increase of the relative intensity and a narrower of the graphite (002) peak, as well as a shift to more positive degrees. Therefore, the graphitization degree of the materials increases in the order: Vulcan < CNC < CNF, being the commercial support the less crystalline. These differences can be explained by the different structure of the materials, as was previously seen by TEM. Vulcan has a structure mainly amorphous, although with a certain crystallinity degree attributed to the turbostratic structure of the primary particles, whereas CNFs and CNCs are more graphitic materials due to the regular-aligned graphitic layers. This observation is confirmed by calculating the graphite interlayer distances (d_{002}), the crystal domain sizes (L_c) and the graphitization degree (g) from the position (2θ) and full width at half maximum (FWHM) of (002) peak for graphite through Bragg, Scherrer and Maire-Mering formulas, respectively. High ordered structures present high values of L_c and g and low values of d_{002} , close to that of perfect graphite

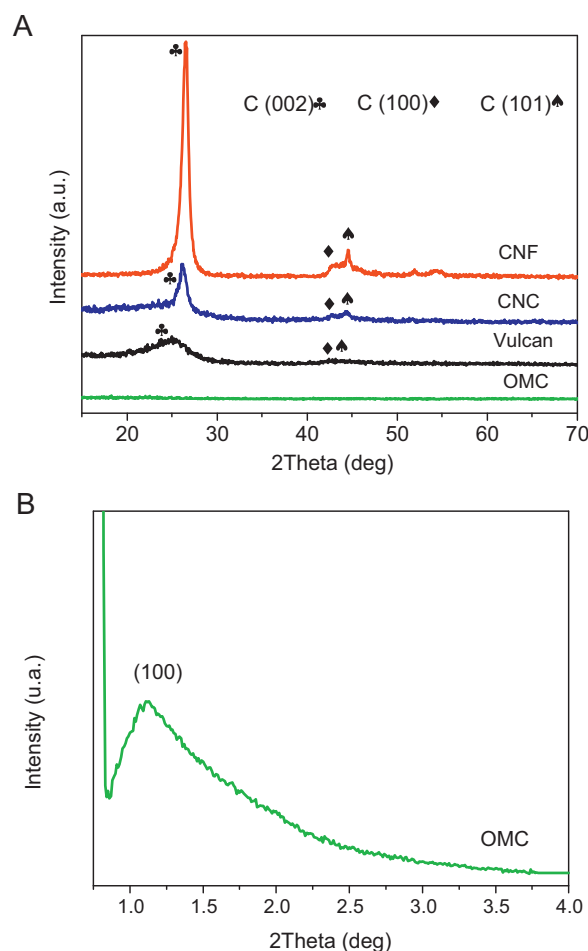


Fig. 2. XRD patterns of carbon supports (A) and XRD pattern at low angles for the OMC sample (B).

(0.3354 nm). According to the values in Table 1, CNFs are the most graphitic material.

In addition, (100) and (101) reflections of the graphite, at $2\theta = 42.4^\circ$ and $2\theta = 44.36^\circ$, are apparent for all the samples. However, in the case of Vulcan, these peaks are hardly discerned, indicative of their more amorphous character.

In the case of the OMC sample, the graphite (002) diffraction line around $2\theta = 25^\circ$ is not perceived, confirming that these materials present an amorphous structure. However, as can be seen in Fig. 2.B, OMCs exhibit a diffraction peak (100), indicating the formation of a highly ordered hexagonal (p6m) mesostructure [50,56]. Through Bragg equation, the interplanar distance (d_{100}) was calculated from the position of the (100) diffraction peak. Taking into account the hexagonal structure of OMCs, the unit cell parameter (a) was obtained. OMCs presented an interplanar distance of 8.02 nm and a distance between carbon cylinders of 9.27 nm, in agreement with values of carbon nanorods (~6 nm) and mesoporous (~3–4 nm) seen by TEM. Similar results have been obtained by other authors [50,56].

Table 1
XRD parameters of carbon supports.

| Sample | 2θ ($^\circ$) | FWHM ($^\circ$) | d_{002} (Å) | L_c (Å) | g (%) |
|--------|------------------------|-------------------|---------------|-----------|---------|
| Vulcan | 25.00 | 4.82 | 3.559 | 1.7 | – |
| CNC | 26.23 | 0.97 | 3.394 | 8.4 | 53 |
| CNF | 26.54 | 0.78 | 3.356 | 10.5 | 97 |

Table 2
Textural and TGA parameters of carbon supports.

| Sample | S_{BET} ($\text{m}^2 \text{g}^{-1}$) | V_{T} ($\text{cm}^3 \text{g}^{-1}$) | D_{p} (nm) | % ash content |
|--------|---|--|---------------------|---------------|
| Vulcan | 237.9 | 0.38 | 10.4 | 2.29 |
| CNF | 75.9 | 0.24 | 11.5 | 4.00 |
| CNC | 233.9 | 0.17 | 4.1 | 5.37 |
| OMC | 812.3 | 0.55 | 3.8 | 3.25 |

Finally, it is remarkable that after the purification treatments of CNFs and CNCs, the catalyst used in their preparation were practically removed as diffraction peaks corresponding to Ni, Co or Cu were almost negligible. In accordance with these results, TGA analysis showed that the ash content, composed of metal and mineral residues was in the range of 4–5% for both materials (Table 2). It is important to note that this residual metal load is encapsulated in the carbon filaments or the nanocoils, and therefore is not accessible for the electrochemical reactions.

Textural properties of the carbon materials obtained by N_2 -physorption are summarized in Table 2. As can be seen, the specific surface area increases in the order: CNFs < CNCs < Vulcan < OMCs, while CNCs show the lowest total pore volume. It is noticeable that OMCs present the highest pore area and volume, which is attributed to their particular preparation method (nanocasting). N_2 adsorption–desorption isotherms of the carbons are given in Fig. 3.A. In all the samples, the obtained isotherms can be classified as type IV (according to the IUPAC

Table 3
EDX, TGA and XRD properties of 20% Pd/C electrocatalysts.

| Sample | % Pd wt. – EDX | % Pd wt. – TGA | d (nm) |
|-----------|----------------|----------------|----------|
| Pd/Vulcan | 17.73 | 19.12 | 3.5 |
| Pd/CNF | 18.81 | 18.89 | 2.9 |
| Pd/CNC | 20.17 | 18.70 | 3.1 |
| Pd/OMC | 19.89 | 18.93 | 3.5 |

classification), as all isotherms present hysteresis loops [57]. The hysteresis loops are associated with capillary condensation in the mesopores, which can be caused by structural pores or spaces between carbon filaments or particles. Different hysteresis loops were obtained for the carbon materials. Vulcan and CNFs present H3 hysteresis (IUPAC), which is characteristic of slit-shaped pores. On the other hand, CNCs show H2 hysteresis, which is distinctive of interconnected pore networks with different shape and size, as the silica (Supelco) used in the synthesis process of this material. Finally, the OMCs hysteresis loop can be classified as type H4, which is characteristic of carbon materials with a size distribution in the range of microporosity or narrow mesoporosity [57,58]. Fig. 3.B shows the pore size distribution (PSD) of the carbon materials. Vulcan and CNFs present wide PSD with two peaks; the first one centered around 2.5 nm for the commercial support and 3.5 nm for the carbon nanofilaments, and followed by a second peak around 30 nm, for both materials. Smaller mesopores are associated with the carbon surface roughness, whereas larger ones (>10 nm) are originated from the interstices between interlaced filaments or carbon particles [59,60]. On the other hand, CNCs and OMCs exhibit narrow PSD, with only one peak around 3.0 nm. However, in the case of CNCs, when the PSD was obtained from the adsorption branch, two peaks centered at 2.5 and 15.0 nm were developed. It could be associated to the presence of bottleneck pores, which would limit N_2 desorption and the available surface area. Additionally, Vulcan and CNFs presented similar average pore sizes, being of 10 nm for Vulcan and 11 for CNF, while CNCs and OMCs exhibited lower pore sizes.

3.2. Physicochemical characterization of the electrocatalysts

The catalysts metal loading was determined by EDX and TGA. Both measurements confirmed that Pd content was similar to the nominal value of 20%, in all the catalysts (Table 3).

TEM micrographs together with particle size distributions can be observed in Fig. 4. In general, a regular distribution of the Pd particles over the carbonaceous supports was observed, with the exception of CNC, where a not uniform dispersion was obtained. Additionally, some particle aggregates can be observed in Fig. 4D, although this agglomeration is not extended over the whole sample. In the case of Pd/CNF, a higher density of particles was detected on the edge of the carbon nanofilaments, as can be seen in Fig. 4C (enclosed figure in the particle size distribution). Narrow size distributions were obtained for Pd catalysts supported on Vulcan, CNF and CNC, whereas Pd/OMC sample exhibited the widest distribution. The average diameter was close to 3–4 nm for all the samples, although when OMCs were used as support, particles with a diameter in the range 6–10 nm were also observed.

Pd/C catalysts were analyzed by XRD technique and their patterns are given in Fig. 5. In all the electrocatalysts three characteristic peaks appeared at $2\theta = 39.4$, 45.6 , 67.4 , which can be assigned to (111), (200) and (220) planes of Pd, respectively, indicating that Pd was deposited with a face centered cubic structure. Pd crystallite size was calculated from Scherrer equation and reported in Table 3. Similar sizes were obtained, with a value around 3–4 nm for all the catalysts, in agreement with the results obtained

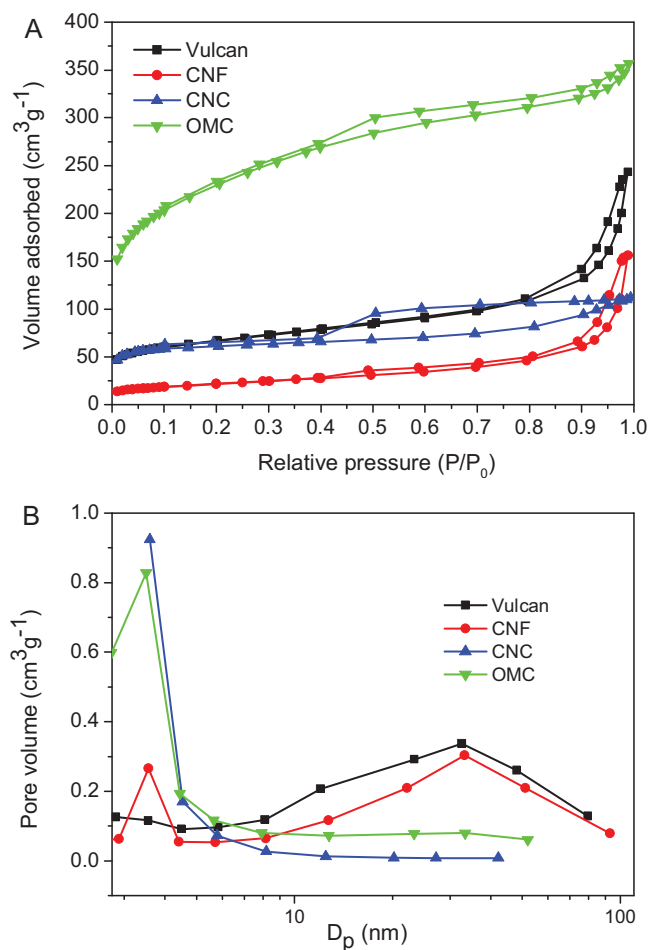


Fig. 3. Nitrogen adsorption–desorption isotherms (A) and PSD of carbon supports (B).

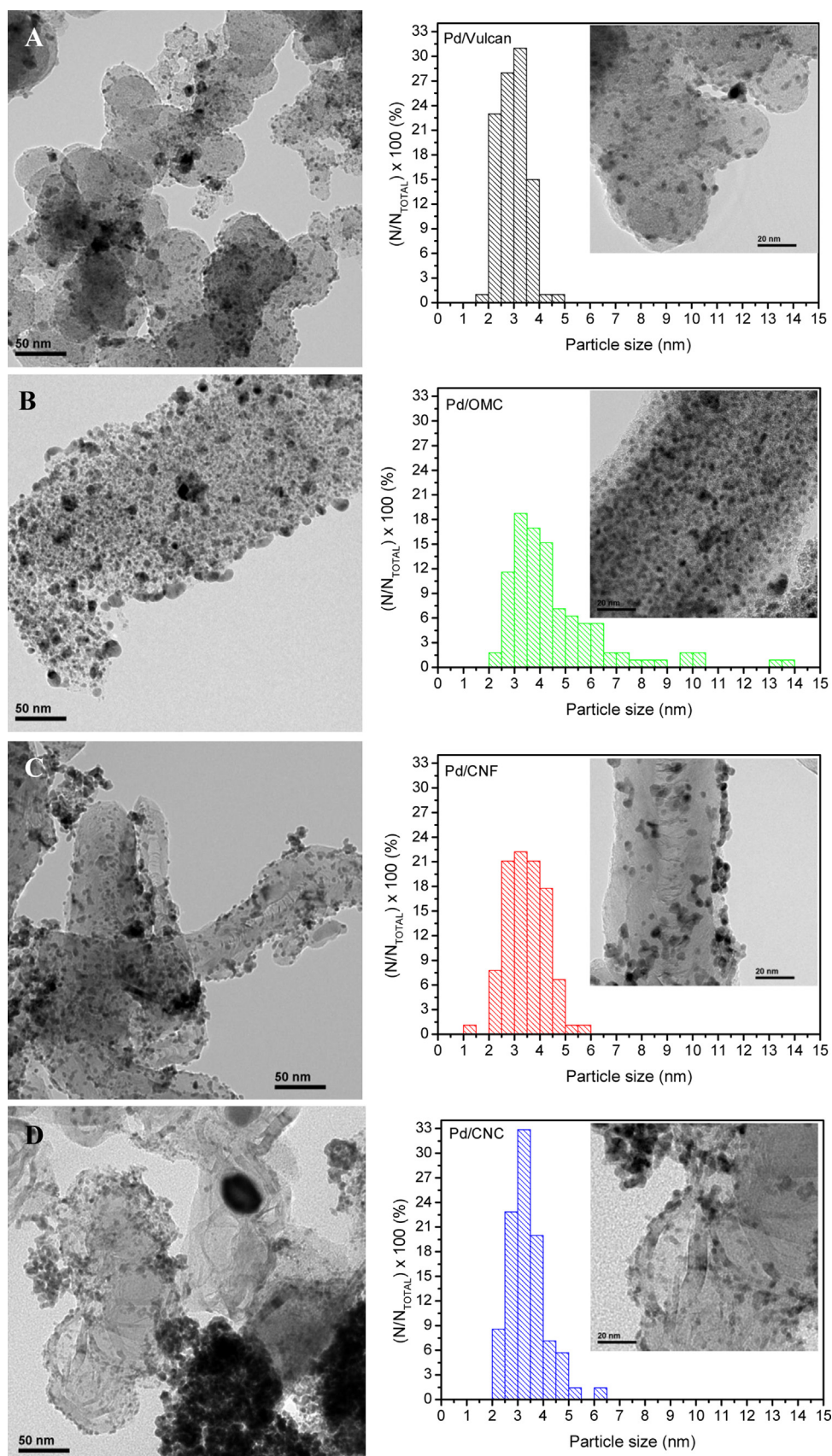


Fig. 4. TEM images and PSD of 20% Pd/C electrocatalysts: Vulcan (A), OMCs (B), CNFs (C) and CNCs (D).

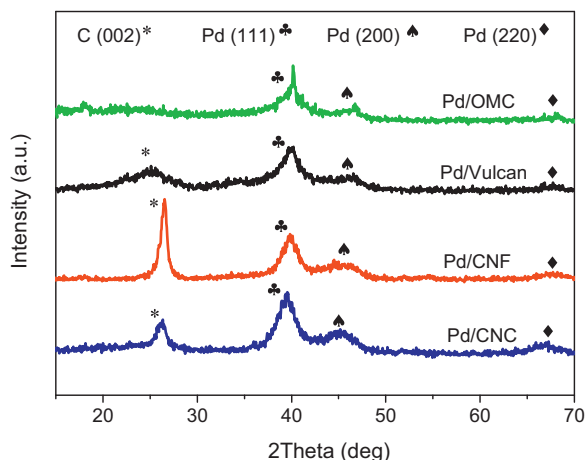


Fig. 5. XRD patterns of 20% Pd/C electrocatalysts.

from TEM images. Additionally, it is noticeable that the diffraction peak at around $2\theta = 25^\circ$, which is associated to the graphite (002) diffraction line of the support, is still observed after the Pd deposition.

3.3. Electrochemical measurements.

The electrochemical behavior of the Pd catalysts was studied in 0.1 M NaHCO_3 , at room temperature and atmospheric pressure by CV. In addition, DEMS experiments were carried out in order to register simultaneously and “in-situ” the formation of molecular hydrogen, which is generated during the CO_2 electrochemical reduction.

First, several potential cycles (not shown) between -0.8 and 0.9 V in 0.1 M NaHCO_3 solution, previously deaerated with Ar, were recorded at 20 mV s^{-1} , to clean and activate the catalyst surface. The voltammetric profile remains similar during the activation step, confirming the stability of the catalysts in the electrolyte. After that, spectro-electrochemical experiments were carried out.

3.3.1. Studies in the -0.8 V to 0.9 V potential range

At the beginning of the experiments, CVs were carried out, at 0.01 V s^{-1} in 0.1 M NaHCO_3 , cycling the potential between -0.8 and 0.9 V in absence (black curves) or in presence (blue curves) of dissolved CO_2 . In this potential region, CO_2 electrochemical reduction does not take place. The curves for each electrode are recorded in Fig. 6.

As can be seen in the black curves (Ar saturated solution), during the cathodic sweep, adsorption/absorption of hydrogen occurs at potentials below -0.3 V, followed by the hydrogen evolution below -0.6 V. In the positive-going potential scan, hydrogen is desorbed and palladium oxides are formed at $E > 0.2$ V. The reduction of these oxides is observed in the negative scan at around -0.2 V. A small shift to more positive potentials (about 50 mV) is observed in presence of CO_2 (blue curves) which can be attributed to the different pHs of the electrolytes (8.4 in the presence of Ar and 6.8 in the presence of CO_2).

Comparing the CVs registered in the absence of CO_2 (black curves), it is remarkable the dependence of the shape of hydrogen desorption region (between -0.8 and 0 V in the positive scan) on the nature of the carbon support. The currents recorded in this potential range are related to hydrogen adsorption/absorption (at the surface and bulk of the Pd particles). This effect is also observed for CVs recorded in a CO_2 saturated solution (blue curves). It is important to note that Pd/OMC catalyst exhibits the highest reduction

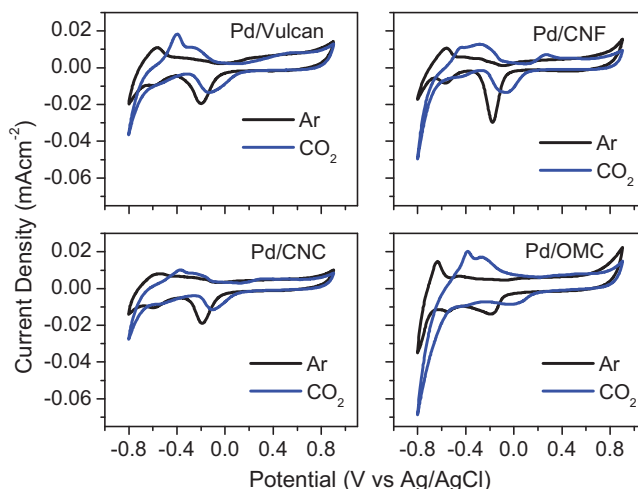


Fig. 6. CVs of Pd/C catalysts in 0.1 M NaHCO_3 ($v = 10 \text{ mV s}^{-1}$, $E_i = 0.2$ V vs. Ag/AgCl). Black curves: Ar saturated solution. Blue curves: CO_2 saturated solution. (For interpretation of the references to color in this figure legend, the reader is referred to the web version of the article.)

currents at -0.8 V, indicating that H_2 evolution is favored onto this sample.

Different reactivity towards the hydrogen evolution reaction of the Pd/C catalysts is evident from comparison of the faradic currents at -0.8 V in the presence and in absence of CO_2 ($I_{\text{CO}_2}/I_{\text{Ar}}$). All catalysts showed a ratio of $I_{\text{CO}_2}/I_{\text{Ar}}$ around 2, with the exception of Pd/CNF sample, in which the value was 3. Thus, the latter catalyst presents the highest reduction currents at this potential which can be ascribed to the presence of high reactive Pd nanoparticles located on the edge of carbon nanofilaments, which could favor hydrogen production in this potential region with CO_2 dissolved in the solution.

Finally, it should be addressed that these Pd/C catalysts display differences in the double layer currents, indicating that samples presented different resistance to charge transfer and capacitance properties, properties that are directly related to the porosity of the carbon materials.

3.3.2. Studies in the -1.4 V to 0.9 V potential range

After the experiments described in Section 3.3.1, DEMS curves were recorded at more negative potentials (between -1.4 V and 0.9 V), with the purpose of studying the electrochemical behavior of the catalysts towards the CO_2 electroreduction process in parallel to the hydrogen evolution, both reactions occurring at these cathodic potentials.

Fig. 7 shows the CVs (upper panel) and the corresponding MSCVs for hydrogen evolution (bottom panel) recorded at 0.01 V s^{-1} in the base electrolyte for the Pd/Vulcan catalyst. The black curve is recorded in the base electrolyte saturated with Ar, while the CO_2 dissolved solution is represented by the blue curve. In the upper panel, it is observed that after saturation with CO_2 (blue curve), a peak around -1.0 V appears during the cathodic scan while the hydrogen region is partly blocked in the anodic sweep. Additionally, two oxidation peaks are developed around 0.1 and 0.3 V. These results suggest that below -0.8 V, CO_2 is being reduced to other species (CO_2)_{red}, which are adsorbed onto the active phase of Pd/C catalyst and oxidized during the anodic scan. According to the bibliography [4,12,15,23] these species are mainly CO_{ad} , which is adsorbed at Pd surface by the reaction:



although other adsorbates, such as COOH_{ad} , COH_{ad} or CH_x could also be formed onto Pd (see later). Consistent with these results,

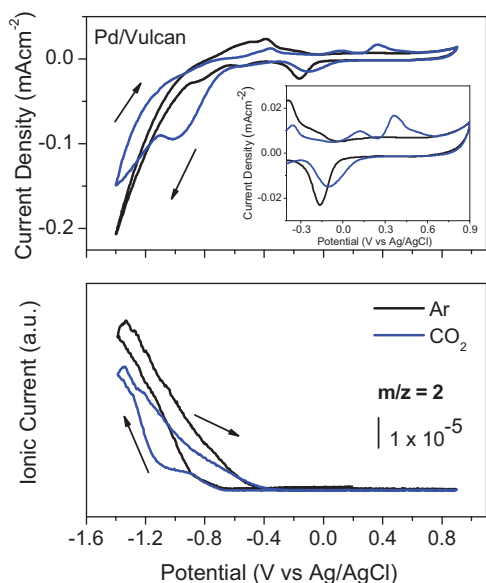


Fig. 7. CVs (upper panel) and MSCV for H_2 , $m/z = 2$ (bottom panel) for Pd/Vulcan catalyst in 0.1 M NaHCO_3 ($v = 10 \text{ mV s}^{-1}$, $E_i = 0.2 \text{ V vs. Ag/AgCl}$). Black curves: Ar saturated solution. Blue curves: CO_2 saturated solution. Inset shows a zoom of the oxidation region. (For interpretation of the references to color in this figure legend, the reader is referred to the web version of the article.)

molecular hydrogen production is significantly decreased by the presence of CO_2 , as it can be observed in the shift of H_2 evolution to more negative potentials, observed in the MSCVs for $m/z = 2$ (Fig. 7, bottom panel blue curve).

Similar results were obtained for the other electrocatalysts and the corresponding CVs are presented in Fig. 8. All samples develop a peak around -1.0 V , which as was mentioned before, is associated to the adsorption of species derived from the CO_2 reduction, and the corresponding oxidation peaks at positive potentials. It is remarkable the high reduction peak observed in the case of Pd/OMC sample (see Fig. 8 blue curve for this catalyst). As mentioned above, this material presented the most significant hydrogen evolution current. Hydrogen plays a very important role in the adsorption of

species derived from CO_2 reduction, since a certain H_{ad} coverage onto the electrode is necessary for the interaction and final formation of “reduced CO_2 ” species. Therefore, higher H_{ad} coverage could lead to more significant CO_2 reduction onto Pd.

On the other hand, with the exception of Pd/Vulcan, hydrogen evolution is completely blocked due to the presence of $(\text{CO}_2)_{\text{red}}$ species, and only for the former material, the cathodic current related to this reaction is still apparent in the CVs. This fact can be explained by a lower coverage of active Pd sites by adspecies at this material.

Finally, comparing the CVs registered in the absence of CO_2 , it is remarkable the dependence of the shape of hydrogen oxidation region (between -0.8 and 0.1 V in the positive scan) on the nature of the carbon support. The currents recorded in this potential range are mainly related to the oxidation of H_2 retained into the carbon materials, since the oxidation charges are significantly larger than a H_{ad} monolayer charge, and consequently, it could not be only produced by adsorbed hydrogen. This H_2 was formed during the cathodic scan and, due to diffusional hindrance it was not released to the electrolyte, remaining into the carbon structure. Then, during the anodic scan, retained hydrogen will be oxidized to protons. As can be observed (see Fig. 8, black curves and see later Fig. 11, black curves), Pd/Vulcan, Pd/CNF and Pd/CNC catalysts presented a H_2 oxidation peak, centered in the (-0.4) to (-0.25) potential range. It is important to remark that the hydrogen oxidation peak is placed at more positive potentials for Pd/CNC ($\approx -0.2 \text{ V}$), in comparison with Pd/Vulcan and Pd/CNF ($\approx -0.35 \text{ V}$). On the other hand, Pd/OMC catalyst shows a large oxidation range from -0.8 V to 0.0 V .

Therefore, it seems that the diffusion and oxidation of this retained hydrogen is more restricted when CNCs or OMCs are used as supports. In this context, the pore structure of the materials allows to explain the results: Vulcan and CNFs present higher average pore sizes, being of 10 and 11 nm respectively, while a value around 4 nm was obtained for CNCs and OMCs. Pore size is a really important parameter to consider in the synthesis of electrocatalysts: on one side, low diameter sizes can produce a pore blockage when the metal nanoparticles are deposited onto the carbon supports; on the other part, diffusion of reactives and products to or from the active sites of the electrocatalysts can be hindered. In this case, textural properties of the support play an important role in the release of produced H_2 out from the carbon structure. Finally, diffusional problems are more evident for Pd/OMC in comparison to Pd/CNC, which could be attributed to the higher hydrogen evolution currents registered for the former catalyst and/or their significant larger surface area (≈ 3.5 times higher for OMC than CNC). As a consequence, larger amounts of hydrogen can be retained inside the carbon structure.

3.3.3. CO and “reduced CO_2 ” strippings

In order to verify if the species formed during the CO_2 electroreduction were irreversibly adsorbed onto the Pd/C electrocatalysts, as well as further investigate onto the nature of these species, stripping voltammograms of CO and “reduced CO_2 ” were performed for all the catalysts.

In the case of CO stripping, CO was adsorbed on the catalyst surface by bubbling this gas through the electrolyte for 30 min at -0.5 V . The excess of CO was then removed from the electrolyte with Ar during 30 min and the potential was cycled between -0.8 and 0.9 V at 0.01 V s^{-1} for three complete cycles. Electrochemical active areas were estimated by the integration of the oxidation of a bridge adsorbed CO monolayer (CO_{ad}), assuming a charge of 210 mC cm^{-2} involved in the process [61,62]. The current densities (A cm^{-2}) given in the text were calculated from these electroactive areas.

CO stripping curves can be observed in Fig. 9 whereas the comparison of the first scan for all the catalysts is shown in Fig. 10.

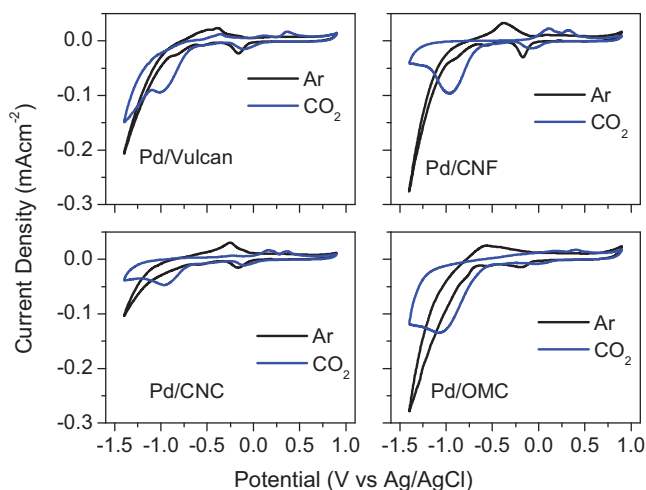


Fig. 8. CVs of Pd/C catalysts in 0.1 M NaHCO_3 ($v = 10 \text{ mV s}^{-1}$, $E_i = 0.2 \text{ V vs. Ag/AgCl}$). Black curves: Ar saturated solution. Blue curves: CO_2 saturated solution. (For interpretation of the references to color in this figure legend, the reader is referred to the web version of the article.)

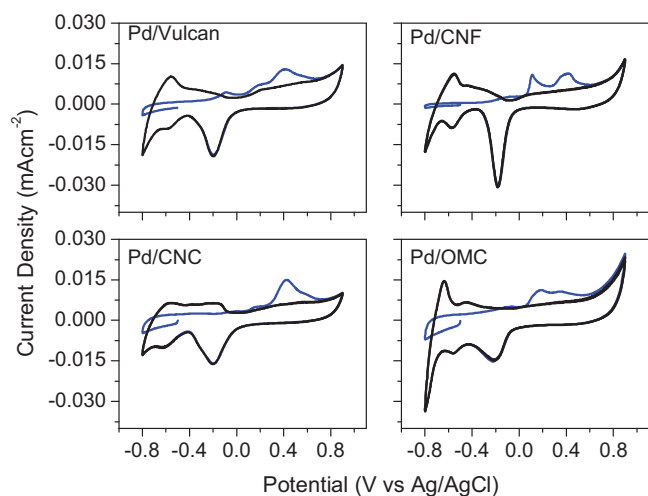


Fig. 9. CO stripping voltammograms (blue line) of Pd/C catalysts in 0.1 M NaHCO₃ ($v = 10 \text{ mV s}^{-1}$, $E_{\text{ad}} = -0.5 \text{ V vs. Ag/AgCl}$).

The hydrogen adsorption/absorption region is completely blocked and two peaks associated to CO oxidation, which are centered at approximately 0.15 and 0.40 V respectively, are depicted in all the CVs. Other authors have obtained a bimodal distribution for CO oxidation on platinum metal nanoparticles supported onto carbon materials [63–65]. It is widely known that the catalytic activity towards this reaction strongly depends on the size and structure of the metal nanoparticles [63,64,66]. Hara and co-workers showed that CO oxidation reaction exhibits distinct structure sensitivity and that the onset potentials of the CO oxidation reaction follow the sequence Pd (100) < Pd (110) < Pd (111) [66]. On the other hand, Maillard et al. reported that Pt nanoparticles with particle size below 3 nm exhibited an increase in the CO oxidation overpotential, whereas larger particles showed a similar behavior than that obtained on a polycrystalline Pt. Additionally, Pt “agglomerates” with high defect sites density exhibited a remarkable activity in comparison to isolated nanoparticles [64]. However, Guerin and co-workers explained this bimodal distribution for CO oxidation by differences in the proportion of terrace sites, which is affected by the metal particle size [63]. An increase in the particle diameter results in a significant decrease in the number of edge sites and an increase of the fraction of terrace sites. Accordingly, they attributed the peak at more negative potentials to CO oxidation on the terraces of larger Pt nanoparticles, whereas the most

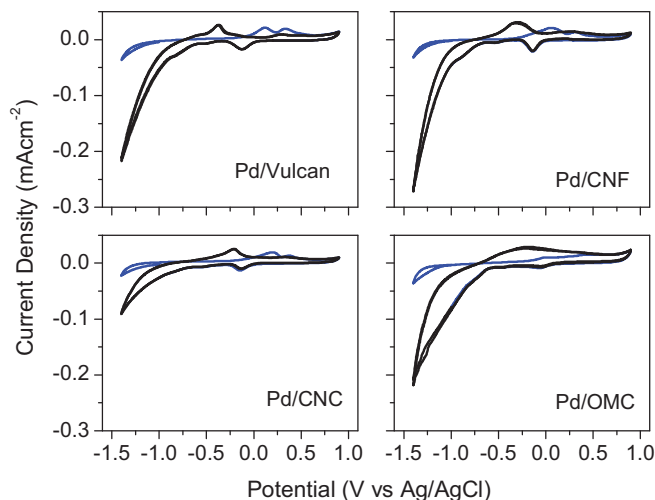


Fig. 11. “Reduced CO₂” stripping voltammograms of Pd/C catalysts in 0.1 M NaHCO₃ ($v = 10 \text{ mV s}^{-1}$, $E_{\text{ad}} = -1.0 \text{ V vs. Ag/AgCl}$).

positive one was associated to CO oxidation on the small-particles edges.

It is remarkable that the intensity of the second peak is higher for the samples Pd/CNC and Pd/Vulcan, while onto catalysts supported on CNFs and OMCs the first contribution becomes more important. Additionally, the onset for CO oxidation shifts to more negative potential for Pd/CNF than for the rest, demonstrating an improved condition for CO stripping from this catalyst surface. This different behavior for Pd catalysts could be attributed to the different nanoparticle size or dispersion onto the carbon supports. As previously observed in TEM images, Pd/OMC displayed larger metal nanoparticles, which could favor the growth of the appropriate Pd crystallographic facets leading to a decrease in the onset potential for CO electrooxidation [66]. On the other hand, Pd/CNF showed a higher density of particles on the edge of the carbon nanofilaments, and consequently, an increase in the amount of border sites contacting two nanoparticles. Therefore, larger particles or high density of Pd may lead to a CO oxidation at more negative potentials, in agreement with the bibliography [63,64,66]. However, Pd/CNC presented a bad dispersion of small size nanoparticles, and in this case, the improvement condition towards CO oxidation was not observed.

After that, “reduced CO₂” strippings were carried out for all the samples as follows: first, CO₂ was bubbled into the NaHCO₃ electrolyte until saturation. Then, the potential was set at -1.0 V for 30 min where CO₂ is reduced forming reduced species that adsorb onto the Pd/C catalysts. Subsequently, the solution was saturated with Ar during 40 min. Finally, the potential was cycled between -1.4 and 0.9 V at 0.01 V s^{-1} for three complete cycles. Fig. 11 shows the “reduced CO₂” stripping voltammograms of the Pd/C catalysts and Fig. 12 a comparison of the first scan of them. In all the samples, two peaks associated to adsorbates derived from the CO₂ electroreduction reaction were observed. The first contribution appears centered in the 0.0 – 0.2 V potential range, followed by a second one centered at about 0.3 – 0.4 V . The intensity of the first peak is higher for all the catalysts, except for the sample Pd/OMC, on which the second contribution becomes more important. It should be mentioned that the hydrogen adsorption/absorption region is completely blocked for all catalysts including Pd/Vulcan, opposite to the results obtained when potential was not set at -1 V for 30 min (Fig. 8A).

A comparison of the CO and “reduced CO₂” strippings for all the Pd/C electrocatalysts can be seen in Fig. 13. It is observed that the oxidation of the reduced species from the CO₂ conversion takes

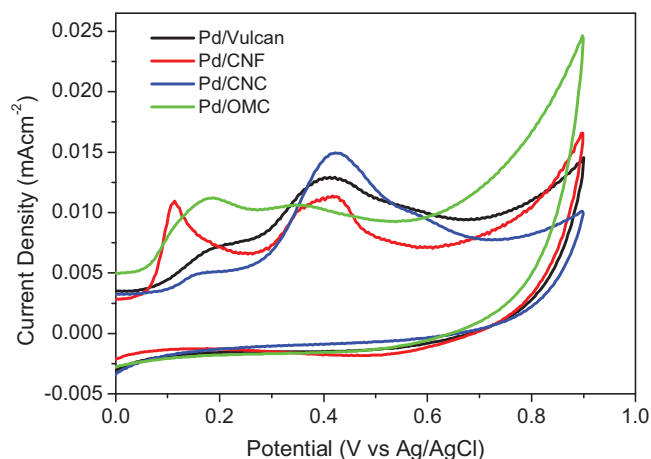


Fig. 10. Comparison of the first scan for CO stripping voltammograms of Pd/C catalysts in 0.1 M NaHCO₃ ($v = 10 \text{ mV s}^{-1}$, $E_{\text{ad}} = -0.5 \text{ V vs. Ag/AgCl}$).

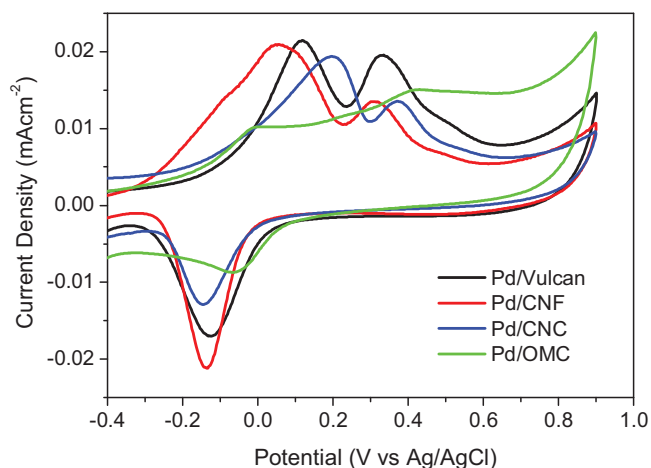


Fig. 12. Comparison of the first scan for “reduced CO₂” stripping voltammograms of Pd/C catalysts in 0.1 M NaHCO₃ ($v = 10 \text{ mV s}^{-1}$, $E_{\text{ad}} = -1.0 \text{ V vs. Ag/AgCl}$).

place at lower potentials than for CO oxidation. In addition, the enclosed area below the “reduced CO₂” stripping voltammogram is much greater, for all the samples. These results suggest that, at potentials below -0.8 V , CO₂ is reduced not only to adsorbed CO, but also other adsorbed species, such as COOH_{ad}, COH_{ad} or CH_x could be obtained. However, the presence of these adsorbates on the Pd surface produces the blocking of the hydrogen region, and consequently, a shift of the hydrogen oxidation features towards more positive values (some kind of adduct may possible be formed between H_{ab} and the adspecies [13,22,23]), partially overlapping with the current of adsorbed species derived from CO₂ reduction. Therefore, part of this higher area observed in the “reduced CO₂” strippings in comparison to the CO ones, could be explained by the oxidation of adsorbed hydrogen. It is important to note that hydrogen atoms absorbed into Pd could take part in the electrochemical reaction, exhibiting a higher chemical reactivity than gaseous hydrogen. K. Ohkawa and co-workers reported an increase in the selectivity for CO₂ reduction after hydrogen was absorbed into a bulk-Pd electrode. This increase was a result from the suppression of H₂ evolution and/or the increase of the reaction rates of CO and HCOOH production [23]. They suggested the participation of adsorbed hydrogen in the reduction of CO₂.

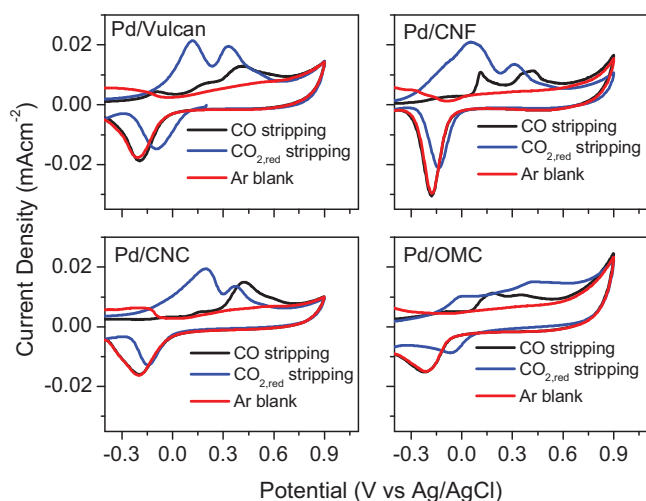
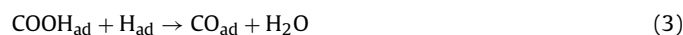


Fig. 13. Comparison of CO and “reduced CO₂” stripping voltammograms for Pd/C catalysts in 0.1 M NaHCO₃ ($v = 10 \text{ mV s}^{-1}$).

The ratio between the oxidation charges associated to “reduced CO₂” and CO ($k = Q_{\text{CO}_2, \text{red}}/Q_{\text{CO}}$) was calculated by the integration of the anodic curves obtained from the stripping voltammograms (Figs. 10 and 12). Higher values of k were obtained for Pd catalysts supported onto CNFs (3.21) followed by the commercial material Vulcan (3.02). Smaller values were calculated for CNC and OMC supported catalysts (2.41 and 2.40, respectively). From these data, it can be concluded that CO_{ad} cannot be the only species on the surface.

If it is assumed that the amount of H_{ab} is similar for all the samples, since the Pd load and the average metal sizes were similar for them, the explanation for these values should imply the presence of different adsorbates onto the electrocatalysts. As was said above (Section 3.3.2) CO_{ad} can be formed at the Pd surface by reaction (1), which probably cannot take place in one step but in a sequence of them:



Additionally, CO_{ad} could interact with adsorbed hydrogen forming COH_{ad}, by the reaction:



These reactions do not represent the adsorption mechanism for CO₂, only try to show that the presence of other adspecies can be easily justified. Also adsorbed hydrogen could be involved in reactions (2)–(4). These adsorbed species when oxidized to CO₂ involved different oxidation charges ($2e^-$ for CO_{ad}, 3 for COH_{ad} and 1 for COOH_{ad}), and accordingly, k values can vary assuming that reaction (2), (3) or (4) are favored for each electrocatalyst. This would suggest differences in the strength of Pd–H_{ad} and/or Pd–H_{ab} depending on the support, which could have an influence on the CO₂ electrochemical reduction process.

Nevertheless, other factors such as the conductivity, textural properties, morphology or structure of the support, as well as the size and distribution of Pd nanoparticles or a good compromise between them, could be also affecting the performance of the Pd-based electrocatalysts towards the electrochemical reduction of CO₂. Additionally, the formation of other adsorbed species or even of volatiles products is not discarded. Other authors have reported the formation of volatile CO and HCOOH at potentials below $-1.4 \text{ V vs. Ag/AgCl}$ [4,15]. Azuma et al. reported also the formation of hydrocarbons traces at higher overpotentials [15].

In order to further investigate about the nature of these species spectro-electrochemical measurements should be carried out. However, this study is out of the scope of the present work: the main objective of the present study is to know if it is possible to electrochemically reduce CO₂ on carbon-supported Pd catalysts and to establish if the carbon support influences on this particular reaction. The product distribution on Pd/C catalysts will be further discussed in a future paper. DEMS analysis of the reduction products is currently underway. Additionally, in order to analyze the influence of the absorbed hydrogen, a study in detail of CO strippings at different potentials is being carried out.

4. Conclusions

Pd catalysts were synthesized for being used in the electroreduction of CO₂ to high-added value products. Different novel nanostructured carbon materials, such as CNCs, CNFs and OMCs, as well as a commercial material, Vulcan XC-72R, were used as support of the catalysts. In this way, the influence of the carbon support on the physicochemical and electrochemical properties of

the catalysts for the CO₂ electroreduction process was studied. On the basis of the results obtained, we concluded as follows:

- Supports presented different morphology and structure. CNCs and CNFs exhibited a crystalline structure with well-aligned graphitic layers. On the other hand, OMCs showed a hexagonal ordered structure, composed of not crystalline carbon. Finally, Vulcan presented an intermediate structure between amorphous and graphitic. Additionally, supports exhibited different textural properties, being OMCs the material that presented the highest specific surface area and pore volume, due to their preparation method (nanocasting technique). CNFs and Vulcan presented wide pore size distribution, while OMCs and CNCs showed narrow distribution, with lower pore sizes (3–4 nm).
- These differences in the physicochemical properties of the supports do not affect significantly the average Pd particle size of catalysts. All catalysts presented a Pd average particle size around 3–4 nm, although when OMCs were used as support, particles with a diameter in the range 6–10 nm were also observed. In general, a good dispersion of the metal phase onto the carbon materials was obtained, with the exception of Pd/CNC sample, where the Pd nanoparticles were not homogeneously distributed. Additionally, Pd/CNF electrocatalyst presented a higher density of particles on the edge of the carbon nanofilaments.
- Catalysts displayed different responses to hydrogen adsorption/absorption, evolution and oxidation processes, which have influence on the CO₂ electroreduction reaction. Additionally, the textural properties of the supports conditioned the diffusion hindrance of H₂ which is partially retained into the carbon structure.
- Cyclic voltammetry studies showed that CO₂ was effectively reduced to other species, which were adsorbed onto Pd, at –1.0 V vs. Ag/AgCl. By comparison of the oxidation charges obtained from CO and “reduced CO₂” strippings, it was concluded that these species were not only CO_{ad}, but also other adsorbates were formed. However, H_{ad} could be also affecting the results, forming some kind of adduct with the adspecies.
- Finally, these electrochemical studies demonstrated that the catalytic activity of Pd/C materials toward the CO₂ electroreduction reaction are influenced by the carbon support used.

Acknowledgments

The authors gratefully acknowledge financial support given by Spanish MINECO (CTQ2011-28913-CO2-01 and 02). S. Pérez-Rodríguez acknowledges Gobierno de Aragón for the DGA grant.

References

- [1] E.A. Batista, M.L.A. Temperini, *Journal of Electroanalytical Chemistry* 629 (2009) 158–163.
- [2] M. Gattrell, N. Gupta, A. Co, *Journal of Electroanalytical Chemistry* 594 (2006) 1–19.
- [3] Y. Hori, H. Wakebe, T. Tsukamoto, O. Koga, *Electrochimica Acta* 39 (1994) 1833–1839.
- [4] M. Azuma, K. Hashimoto, M. Hiramoto, M. Watanabe, T. Sakata, *Journal of the Electrochemical Society* 137 (1990) 1772–1778.
- [5] Y. Hori, *Handbook of Fuel Cells*, John Wiley & Sons, Ltd, 2010.
- [6] B. Innocent, D. Pasquier, F. Ropital, F. Hahn, J.M. Léger, K.B. Kokoh, *Applied Catalysis B: Environmental* 94 (2010) 219–224.
- [7] Y. Hori, H. Konishi, T. Futamura, A. Murata, O. Koga, H. Sakurai, K. Oguma, *Electrochimica Acta* 50 (2005) 5354–5369.
- [8] H. De Jesús-Cardona, C. Del Moral, C.R. Cabrera, *Journal of Electroanalytical Chemistry* 513 (2001) 45–51.
- [9] S. Kaneco, N.H. Hiei, Y. Xing, H. Katsumata, H. Ohnishi, T. Suzuki, K. Ohta, *Electrochimica Acta* 48 (2002) 51–55.
- [10] S. Kaneco, N.H. Hiei, Y. Xing, H. Katsumata, H. Ohnishi, T. Suzuki, K. Ohta, *Journal of Solid State Electrochemistry* 7 (2003) 152–156.
- [11] B. Jermann, J. Augustynski, *Electrochimica Acta* 39 (1994) 1891–1896.
- [12] D. Kolbe, W. Vielstich, *Electrochimica Acta* 41 (1996) 2457–2460.
- [13] M. Grdeń, A. Paruszeńska, A. Czerwiński, *Journal of Electroanalytical Chemistry* 502 (2001) 91–99.
- [14] S. Taguchi, A. Aramata, M. Enyo, *Journal of Electroanalytical Chemistry* 372 (1994) 161–169.
- [15] M. Azuma, K. Hashimoto, M. Watanabe, T. Sakata, *Journal of Electroanalytical Chemistry* 294 (1990) 299–303.
- [16] M.C. Arévalo, C. Gomis-Bas, F. Hahn, B. Beden, A. Arévalo, A.J. Arvia, *Electrochimica Acta* 39 (1994) 793–799.
- [17] A. Rodes, E. Pastor, T. Iwasita, *Journal of Electroanalytical Chemistry* 369 (1994) 183–191.
- [18] A. Rodes, E. Pastor, T. Iwasita, *Journal of Electroanalytical Chemistry* 377 (1994) 215–225.
- [19] Y.B. Vassiliev, V.S. Bagotzky, N.V. Osetrova, A.A. Mikhailova, *Journal of Electroanalytical Chemistry* 189 (1985) 311–324.
- [20] B. Beden, A. Bewick, M. Razaq, J. Weber, *Journal of Electroanalytical Chemistry* 139 (1982) 203–206.
- [21] P.A. Christensen, A. Hamnett, A.V.G. Muir, N.A. Freeman, *Journal of Electroanalytical Chemistry* 288 (1990) 197–215.
- [22] A. Czerwiński, S. Zamponi, R. Marassi, *Journal of Electroanalytical Chemistry and Interfacial Electrochemistry* 304 (1991) 233–239.
- [23] K. Ohkawa, K. Hashimoto, A. Fujishima, *Journal of Electroanalytical Chemistry* 345 (1993) 445–456.
- [24] A. Rodes, E. Pastor, T. Iwasita, *Journal of Electroanalytical Chemistry* 373 (1994) 167–175.
- [25] R.P.S. Chaplin, A.A. Wragg, *Journal of Applied Electrochemistry* 33 (2003) 1107–1123.
- [26] E.V. Kondratenko, G. Mul, J. Baltrusaitis, G.O. Larrázabal, J. Pérez-Ramírez, *Energy and Environmental Science* 6 (2013) 3112–3135.
- [27] F.A. Lewis, *The Palladium-Hydrogen Systems*, Academic Press, New York, 1967.
- [28] K. Hara, A. Kudo, T. Sakata, *Journal of Electroanalytical Chemistry* 391 (1995) 141–147.
- [29] S. Nakagawa, A. Kudo, M. Azuma, T. Sakata, *Journal of Electroanalytical Chemistry* 308 (1991) 339–343.
- [30] B. Eneau-Innocent, D. Pasquier, F. Ropital, J.M. Léger, K.B. Kokoh, *Applied Catalysis B: Environmental* 98 (2010) 65–71.
- [31] K. Ohta, M. Kawamoto, T. Mizuno, D.A. Lowy, *Journal of Applied Electrochemistry* 28 (1998) 717–724.
- [32] Y.B. Vassiliev, V.S. Bagotzky, O.A. Khazova, N.A. Mayorova, *Journal of Electroanalytical Chemistry* 189 (1985) 295–309.
- [33] C. Genovese, C. Ampelli, S. Perathoner, G. Centi, *Journal of Energy Chemistry* 22 (2013) 202–213.
- [34] M.N. Mahmood, D. Mashed, C.J. Harty, *Journal of Applied Electrochemistry* 17 (1987) 1159–1170.
- [35] S. Pérez-Rodríguez, G. García, L. Calvillo, V. Celorrio, E. Pastor, M.J. Lázaro, *International Journal of Electrochemistry* 2011 (2011).
- [36] G. Centi, S. Perathoner, Z.S. Rak, *Applied Catalysis B: Environmental* 41 (2003) 143–155.
- [37] M. Gangeri, S. Perathoner, S. Caudo, G. Centi, J. Amadou, D. Bégin, C. Pham-Huu, M.J. Ledoux, J.P. Tessonnier, D.S. Su, R. Schlögl, *Catalysis Today* 143 (2009) 57–63.
- [38] S. Perathoner, M. Gangeri, P. Lanzafame, G. Centi, *Kinetics and Catalysis* 48 (2007) 877–883.
- [39] G. Centi, S. Perathoner, G. Winè, M. Gangeri, *Green Chemistry* 9 (2007) 671–678.
- [40] G. Centi, S. Perathoner, *Topics in Catalysis* 52 (2009) 948–961.
- [41] Y. Hori, K. Kikuchi, S. Suzuki, *Chemistry Letters* (1985) 1695–1698.
- [42] C.W.B. Bezerra, L. Zhang, H. Liu, K. Lee, A.L.B. Marques, E.P. Marques, H. Wang, J. Zhang, *Journal of Power Sources* 173 (2007) 891–908.
- [43] D. Sebastián, I. Suelves, R. Moliner, M.J. Lázaro, *Carbon* 48 (2010) 4421–4431.
- [44] D. Sebastián, I. Suelves, R. Moliner, M.J. Lázaro, A. Stassi, V. Baglio, A.S. Arico, *Applied Catalysis B: Environmental* 132–133 (2013) 22–27.
- [45] D. Sebastián, I. Suelves, E. Pastor, R. Moliner, M.J. Lázaro, *Applied Catalysis B: Environmental* 132–133 (2013) 13–21.
- [46] V. Celorrio, L. Calvillo, M.V. Martínez-Huerta, R. Moliner, M.J. Lázaro, *Energy and Fuels* 24 (2010) 3361–3365.
- [47] V. Celorrio, L. Calvillo, S. Pérez-Rodríguez, M.J. Lázaro, R. Moliner, *Microporous and Mesoporous Materials* 142 (2011) 55–61.
- [48] L. Calvillo, V. Celorrio, R. Moliner, P.L. Cabot, I. Esparbè, M.J. Lázaro, *Microporous and Mesoporous Materials* 116 (2008) 292–298.
- [49] M.J. Lázaro, L. Calvillo, E.G. Bordejé, R. Moliner, R. Juan, C.R. Ruiz, *Microporous and Mesoporous Materials* 103 (2007) 158–165.
- [50] Y. Meng, D. Gu, F. Zhang, Y. Shi, H. Yang, Z. Li, C. Yu, B. Tu, D. Zhao, *Angewandte Chemie - International Edition* 44 (2005) 7053–7059.
- [51] J. Biscoe, B.E. Warren, *Journal of Applied Physics* 13 (1942) 364–371.
- [52] J.L. Langford, A.J.C. Wilson, *Journal of Applied Crystallography* 11 (1978) 102–113.
- [53] D. Torres, J.L. Pinilla, M.J. Lázaro, R. Moliner, I. Suelves, *International Journal of Hydrogen Energy* 39 (2014) 3698–3709.
- [54] J. Maire, J. Mering, *Chemistry and Physics of Carbon* 6 (1970) 125–189.
- [55] G. García, J. Flórez, O. Guillén-Villafuerte, J.L. Rodríguez, E. Pastor, in preparation.
- [56] S. Song, K. Wang, Y. Liu, C. He, Y. Liang, R. Fu, D. Wu, Y. Wang, *International Journal of Hydrogen Energy* 38 (2013) 1405–1412.
- [57] H. Marsh, F. Rodríguez-Reinosos, Elsevier Science & Technology Books, 2006.
- [58] G. Leofanti, M. Padovan, G. Tozzola, B. Venturini, *Catalysis Today* 41 (1998) 207–219.

- [59] T.V. Reshetenko, L.B. Avdeeva, Z.R. Ismagilov, V.V. Pushkarev, S.V. Cherepanova, A.L. Chuvilin, V.A. Likholobov, *Carbon* 41 (2003) 1605–1615.
- [60] S.K. Shaikhutdinov, V.I. Zaikovskii, L.B. Avdeeva, *Applied Catalysis A: General* 148 (1996) 123–133.
- [61] M.C. Arévalo, J.L. Rodríguez, E. Pastor, *Journal of Electroanalytical Chemistry* 505 (2001) 62–71.
- [62] M.C. Arévalo, J.L. Rodríguez, E. Pastor, *Journal of Electroanalytical Chemistry* 472 (1999) 71–82.
- [63] S. Guerin, B.E. Hayden, C.E. Lee, C. Mormiche, J.R. Owen, A.E. Russell, B. Theobald, D. Thompsett, *Journal of Combinatorial Chemistry* 6 (2004) 149–158.
- [64] F. Maillard, S. Schreier, M. Hanzlik, E.R. Savinova, S. Weinkauff, U. Stimming, *Physical Chemistry Chemical Physics* 7 (2005) 385–393.
- [65] S. Sun, Z. Jusys, R.J. Behm, *Journal of Power Sources* 231 (2013) 122–133.
- [66] M. Hara, U. Linke, T. Wandlowski, *Electrochimica Acta* 52 (2007) 5733–5748.